ISSN 0001-4338, Izvestiya, Atmospheric and Oceanic Physics, 2010, Vol. 46, No. 3, pp. 347–359. © Pleiades Publishing, Ltd., 2010.
Original Russian Text © V.G. Bondur, Yu.V. Grebenyuk, E.V. Ezhova, V.I. Kazakov, D.A. Sergeev, I.A. Soustova, Yu.I. Troitskaya, 2010, published in Izvestiya AN. Fizika Atmosfery i Okeana, 2010, Vol. 46, No. 3, pp. 376–389.

Surface Manifestations of Internal Waves Investigated by a Subsurface Buoyant Jet: Part 2. Internal Wave Field

V. G. Bondur[a], Yu. V. Grebenyuk[a], E. V. Ezhova[b], V. I. Kazakov[b], D. A. Sergeev[b], I. A. Soustova[b], and Yu. I. Troitskaya[b]

[a] *Aerokosmos Scientific Center of Aerospace Monitoring, Gorokhovskii per. 4, Moscow, 105064 Russia*
e-mail: vgbondur@aerocosmos.info

[b] *Institute of Applied Physics, Russian Academy of Sciences, ul. Ul'yanova 46, Nizhni Novgorod, 603950 Russia*
e-mail: yuliya@hydro.appl.sci-nnov.ru

Received August 12, 2009

Abstract—In a large test reservoir with artificial temperature stratification at the Institute of Applied Physics, Russian Academy of Sciences, a major simulation of internal wave actuation by buoyant turbulent jets generated by wastewater flows from underwater collector diffusers in conditions of temperature stratification with deep and shallow thermocline has been performed. Using a modification of the particle tracing velocimetry (PTV) method in the stratification mode with shallow thermocline, the velocities of currents generated by internal waves at the surface of the water area are measured. A theoretical model is developed describing the fields of internal waves in the presence of jet stream. Dispersion relations and structures of lower (first and second) modes of internal waves in the stratified basin for different rates of liquid outflow from the collector model are obtained. The experimentally measured field of isothermal shifts with respect to the system of characteristic modes of internal waves is decomposed. A mixed regime of internal wave actuation with the simultaneous existence of the first and second modes is observed. The characteristics of perturbations in the liquid column and on its surface are compared. This analysis allows us to prove that the velocity fields on the surface are indeed surface manifestations of internal waves.

DOI: 10.1134/S0001433810030084

1. INTRODUCTION

Deepwater sinks carry significant anthropogenic load on the coastal area, affecting its total mass exchange, hydrodynamics, and the state of the ecosystem. A comprehensive investigation of these processes includes mathematically modeling the dynamics of submerged turbulent jets [1–5], contact measurements [6], and remote aerospace monitoring methods [7–10] based detecting and estimating the surface manifestations of underwater sinks. Currently, the physical reasons for surface manifestations of deepwater sinks are not clearly understood. Along with the rise of wastewater to the surface, the mechanisms conditioned by surface deformation by rising eddies or internal waves have been discussed [7, 8, 10]; in [9], the surface manifestations of underwater sinks are explained by a complex interaction of turbulence, internal waves, tidal currents, and bottom topography.

In the first part of this study [11] we studied the hydrodynamic processes near the underwater collector of disposal system using major laboratory simulation and proposed a way to generate interval waves. Here, the source of these waves is self-oscillations of buoyant jets interacting with pycnocline [11–13]. The waves are radiated if the frequency of self-oscillations is lower than the buoyancy frequency of stratified liquid. A large laboratory simulation of the hydrodynamics of the underwater disposal system shows the efficiency of this internal-wave actuation method for typical parameters of disposal systems and coastal-area stratification.

The main aim of the second part of this work is to conduct a detailed study of the fields of internal waves radiated by a source near the collector. The method of investigations includes a study of the fields of internal waves radiated by the disposal system in large-simulation conditions implemented on the basis of the large thermally stratified test reservoir (LTSR) at the Institute of Applied Physics, Russian Academy of Sciences [11, 12], as well as their theoretical description.

We obtained dispersion relations and structures of characteristic modes of wave actuations in liquid with density and velocity profiles obtained in the experiment. We interpreted the vertical structure of the temperature field as a superposition of normal modes of internal waves, explaining a number of its features observed in the experiment.

This work has the following structure. Section 2 briefly describes the main features of the experimental setup, the characteristics of the measuring system and

experimental technique, and the background stratification and flow fields in the basin. Section 3 analyzes the results obtained in the LTSR. The structure of internal wave fields and their spectral composition are given. Section 4 describes a theoretical model for the field of internal waves with a calculation of the structure and dispersion characteristics of modes. Section 5 presents a mode and dispersion analysis of the fields of temperature oscillations obtained experimentally and, based on this, the observed oscillations are interpreted as fields of internal waves.

2. MAJOR ELEMENTS OF EXPERIMENTAL SETUP AND MEASUREMENT SYSTEM; BACKGROUND STRUCTURE OF TEMERATURE AND VELOCITY FIELDS

In the LTSR, we performed two series of experiments to investigate the fields of internal waves actuated by turbulent buoyant jets. In the first series, the level of maximum gradient of temperature was located at a depth of 45–50 cm (deepwater thermocline) and, in the second series, at a depth of 13–15 cm (shallow thermocline). The schematic of the experimental setup is shown in Fig. 1. The water-temperature oscillations caused by jet rise were fixed with the help of a garland consisting of 14 thermistors. The profiles of current velocities were measured by a three-component Doppler velocimeter.

In the series of experiments with shallow thermocline, we measured the velocity of surface currents induced by buoyant jets. This was done using the particle tracing velocimetry (PTV) method [14]. Here, the limited area of observation of the water-basin surface was seeded by black polyethylene particles with a characteristic size of 1.5 mm to create a contrast with the white bottom. The motion of particles was imaged from the top with a digital video camera, and the resulting time series of images were then processed on a computer.

In view of the construction peculiarities of experimental installations, the measurement areas of surface currents and sensor garlands fixing the temperature oscillations were allocated along the basin at distances of 1 and 2 m in different experiments. This made it possible to estimate the group velocity of internal waves by the time that perturbations appeared on the garland of thermistors and in the area seeded by particles (see Section 4). A detailed description of the technique of current velocity on the surface can be found in Section 3 of this study.

Below, the experiments performed in conditions of deepwater thermocline are related to Series D; the experiments performed in conditions of shallow thermocline, when the temperature sensors and particle observation area were allocated at a distance of 1 m (2 m), are related to Series S1 (S2). The total number of experiments was 25 in Series D, 8 in Series S1, and 6 in Series S2.

For each implementation, using experimental data, we calculated the time-averaged profiles of background stratification, which are approximated well by a function of the form

$$T = \frac{\Delta T}{2}\tanh\left(\frac{z + z_{rysp}}{\Delta H}\right) + T_{avg}, \quad (1)$$

where ΔT is the value of temperature jump, z_{rysp} is the position of the mid-thermocline relative to the basin surface, ΔH is the half-thickness of the thermocline, and T_{avg} is the average temperature in the jump area (see Fig. 2). By the known stratification profile, the profiles of buoyancy frequency were obtained using special-purpose software:

$$N(z) = -\frac{g}{\rho_0}\frac{d\rho_0}{dz}. \quad (2)$$

Using velocimeter indications, the average profiles of velocity were determined for each implementation. Examples of the velocity profiles are shown in Fig. 2. It can be seen from the figures that the velocity profiles in the given area are described well by the function

$$U_0(z) = \frac{1}{2}(U_{\max} + U_{\min})\left(1 - \frac{U_{\max} - U_{\min}}{U_{\max} + U_{\min}}\tanh\left(\frac{z}{\Delta h}\right)\right), \quad (3)$$

where $U_{\max}$ is the maximum value of velocity in the jet, $U_{\min}$ is the minimum value of velocity, and Δh is the thickness of mixing layer.

It can be seen from Table 1 that $U_{\min} < 0$; i.e., there is weak countercurrent in the upper layer. This countercurrent can be caused by the nonuniform warming of liquid by the heat-exchange system or it may be somehow related to the motion of the jet itself. The countercurrent increases the velocity gradient and thus affects the mode structure.

The parameters of experiments for all series are presented in Table 1.

3. INTERNAL WAVE STRUCTURE

Based on the indications of the temperature sensor, we calculated the isotherms characterizing the shifts of liquid particles relative to equilibrium level and their spectra, as well as the rms values. Figure 3a shows the isotherms corresponding to temperatures from 9 to 20°C with a step of 1°C for a velocity $V_0 = 100$ cm/s of liquid outflow from the diffuser (Series D). The dotted lines indicate four isotherms in the range from 9 to 12°C.

Similar examples for Series S are shown in Fig. 3b (here, the isotherms correspond to temperatures from 10 to 20°C). It can be seen from the figures that the rising jet actuates intense oscillations of temperature (isotherm shifts).

Figures 4a and 4b show the spectra of isotherm shifts for a velocity of liquid outflow from the collector

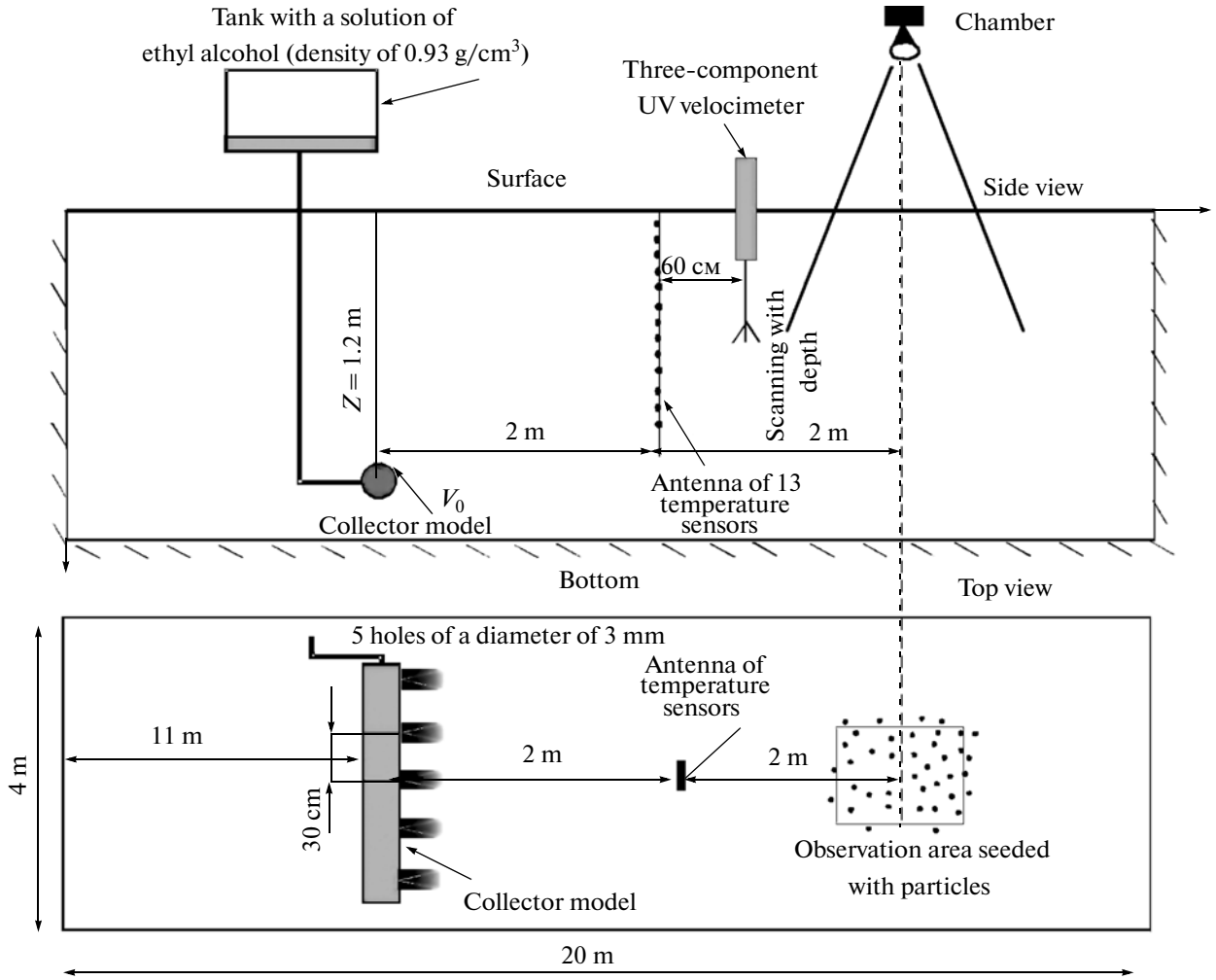

Fig. 1. General schematic of LTSR experiments with the location of temperature and velocity sensors before the surface observation area.

of 100 cm/s obtained by ensemble averaging over all implementations of the given velocity and stratification ((a) corresponds to Series D and (b) corresponds to Series S). The isotherm spectra have a clearly expressed maximum in the frequency range from $f_0 = 0.02$ Hz to $f_{max} = 0.05$ Hz, which is lower than the maximum buoyancy frequency; i.e., the spectral maximum is located in the propagation of internal waves. The dispersion of shifts of each isotherm was calculated by the formula $\langle \sigma^2 \rangle = \int_{f_0}^{f_{max}} Sp(f)df$, where $Sp(f)$ is the spectrum of isotherm shifts relative to the mean level. Examples of the rms profiles of $\sigma^2(z)$ corresponding to the velocity of liquid outflow from the collector model of 100 cm/s for Series D and S are shown in Fig. 2. The profile of $\sigma^2(z)$ characterizes the distribution of the oscillation amplitude by depth, which is determined by the structure of the internal wave field. The dependence of $\sigma^2(z)$ has two maxima: in the thermocline and in the jet. Here, the maximum in the thermocline is expressed weakly in comparison with the maximum in the jet.

4. THEORETICAL MODEL OF THE FIELD OF INTERNAL WAVES NEAR AN UNDERWATER DISPOSAL SYSTEM

4.1. Main Equations

The LTSR experiments indicated that the buoyant liquid outflow from the collector model is characterized by the generation of shear flow with the jet profile of the velocity localized below the thermocline. The velocity on the jet axis constituted approximately 2 cm/s (see Fig. 2). As is shown below, this value is comparable to the velocity of short-period internal waves actuated in the basin by a jet stream. In view of this, one can expect that this jet stream will significantly influence the dispersion properties of internal waves and the form of their characteristic modes.

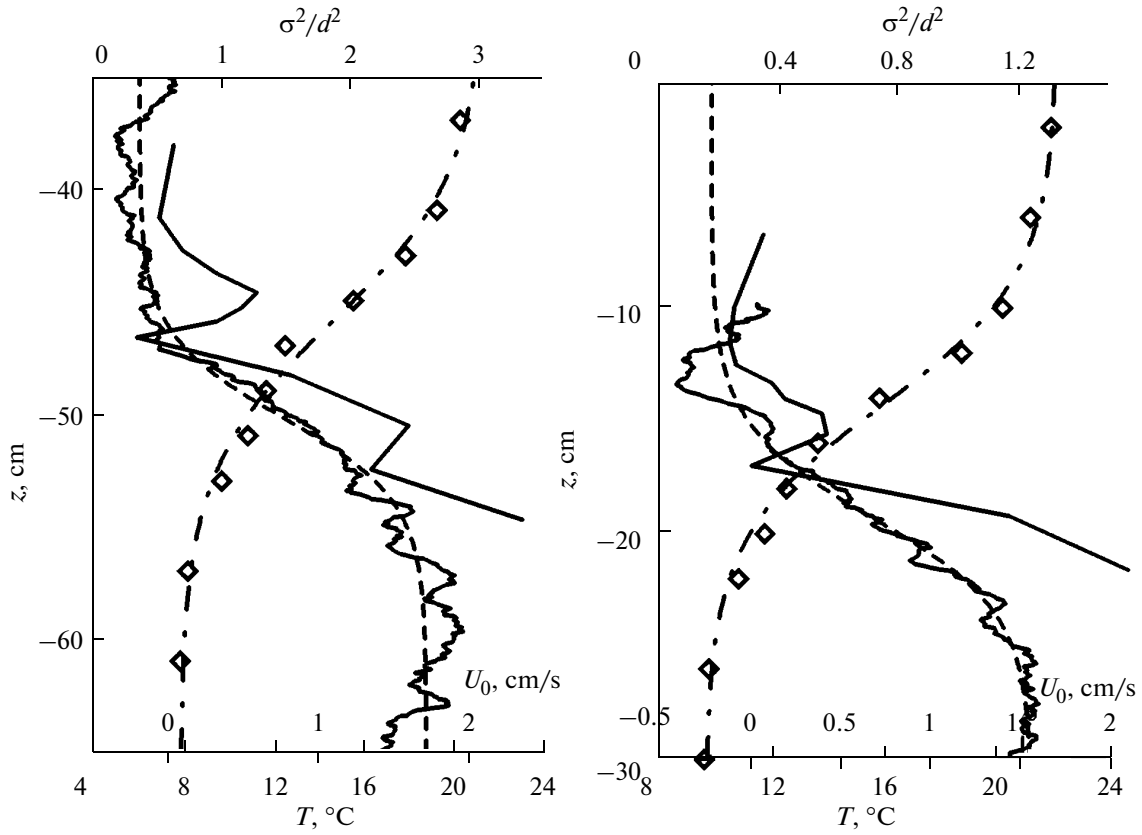

Fig. 2. Average flow characteristics: operating profile of stratification (rhombus), and its approximation (dashed and dotted line), profile of mean jet velocity (solid line) and its approximation (dotted line); rms profiles: (a) Series D and (b) Series S2.

To calculate these characteristics, in this section we develop a theoretical model for the field of internal waves in the presence of a jet stream. This model also will be used for interpreting measurement data on current velocities on the surface (see Section 3 of this study [15]): based on measured isotherm deviations in the liquid column, we will calculate the current velocity on the water surface and compare it with data obtained by the PTV method.

Let us consider the following statement of the problem. Let the basin be filled with stratified liquid with given unperturbed profiles of density $\rho_0(z)$ and buoyancy frequency $N(z)$. In this case, the liquid column includes a shear flow with a velocity profile $U_0(z)$ (see Fig. 2).

For a further description, we use an approximation of ideal incompressible flow (i.e., Euler equation), conditions of incompressibility, and mass conservation law:

$$\begin{gathered}\rho_0\left(\frac{\partial \mathbf{u}}{\partial t}+(\mathbf{u},\nabla)\mathbf{u}\right)=-\nabla p-\rho_1\mathbf{g},\\ \frac{\partial \rho_1}{\partial t}+(\mathbf{u},\nabla)\rho_1+w\frac{d\rho_0}{dz}=0,\\ \operatorname{div}\mathbf{u}=0.\end{gathered}\tag{4}$$

We search the solution of system (4) as a superposition of the unperturbed current and wave perturbations:

$$\begin{gathered}\mathbf{u}=U_0(z)\mathbf{x}_0+\mathbf{u}_1,\\ p=p_0+p_1,\\ \rho=\rho_0+\rho_1.\end{gathered}$$

The linearization of the system of equations with respect to perturbations yields

$$\begin{gathered}\rho_0\left(\frac{\partial u_1}{\partial t}+U_0\frac{\partial u_1}{\partial x}+w_1\frac{\partial U_0}{\partial z}\right)=-\frac{\partial p_1}{\partial x},\\ \rho_0\left(\frac{\partial w_1}{\partial t}+U_0\frac{\partial w_1}{\partial x}\right)=-\frac{\partial p_1}{\partial z}-\rho_1 g,\\ \rho_0\left(\frac{\partial \rho_1}{\partial t}+U_0\frac{\partial \rho_1}{\partial x}\right)+w_1\frac{d\rho_0}{dz}=0,\\ \frac{\partial u_1}{\partial x}+\frac{\partial w_1}{\partial z}=0,\end{gathered}\tag{5}$$

where $\mathbf{u}=\{u,w\}$, u and w are the horizontal and vertical velocities of perturbations, respectively; and $\rho_0(z)$ is the unperturbed profile of density.

In system (5), let us turn to the variables of vorticity $\boldsymbol{\Omega}$ and stream function ψ. Then, the velocity compo-

Table 1.

Series of experiments	D	S1	S2
Jet embedding relative to basin surface H_u, cm	47.7–52.6	16.5–17.6	15.6–20.2
Half-width of thermocline ΔH, cm	5.9–7.6	3.9–4.7	5.1–6.9
Half-width of jet Δh, cm	2.5–5.7	2.4–3.9	4.0–6.2
Jet embedding relative to the thermocline center z^*, cm	4.3–7.8	4.5–5.6	5.1–6.6
Maximum buoyancy frequency N_0, rad/s	0.346–0.414	0.456–0.508	0.423–0.442
Maximum jet velocity $U_{\max}$, cm/s	1.40–2.24	0.65–0.80	1.11–1.97
Minimum jet velocity $U_{\min}$, cm/s	–0.08–(–0.33)	–0.04–(–0.12)	–0.07–(–0.30)
$\gamma = \left(\frac{\Delta H}{\Delta h}\right)$	1.16–2.72	1.14–1.67	1.04–1.32
$\xi^* = \frac{z^*}{\Delta H}$	0.56–1.26	1.16–1.22	0.73–1.3
$R = \frac{N_0^2(\Delta H)^2}{U_m^2}$	1.26–3.32	6.74–9.19	1.9–3.93
$\beta = \frac{U_{\max} - U_{\min}}{U_{\max} + U_{\min}}$		1.13–1.35	

nents are expressed through ψ as $u = \frac{\partial \psi}{\partial z}$, $w = -\frac{\partial \psi}{\partial x}$, and system (5) takes the form

$$\frac{\partial^2 \mathbf{\Omega}}{\partial t^2} + N^2 \frac{\partial^2 \mathbf{\psi}}{\partial x^2} + U_0 \frac{\partial^2 \mathbf{\Omega}}{\partial x \partial t} - U_0'' \frac{\partial^2 \mathbf{\psi}}{\partial x \partial t} = 0, \quad \frac{\partial^2 \psi}{\partial x^2} + \frac{\partial^2 \psi}{\partial z^2} = \mathbf{\Omega}, \tag{6}$$

where $N(z) = -\frac{g}{\rho_0}\frac{d\rho_0}{dz}$ is the profile of buoyancy frequency.

The problem is solved by the method of normal modes. Let us assume that the solution is proportional to $\exp\{i(kx - \omega t)\}$; then, system (6) transforms into the Taylor–Goldstein equation [16]

$$\frac{\partial^2 \psi}{\partial z^2} - k^2 \psi + \frac{N^2}{(U_0 - c)^2}\psi - \frac{U_0''}{(U_0 - c)}\psi = 0. \tag{7}$$

Here, $c = \frac{\omega}{k}$ is the phase velocity of the wave.

The boundary conditions at the bottom and surface of the basin are $w(H_u) = w(H_d) = 0$ and, consequently, we have

$$\psi(H_u) = \psi(H_d) = 0. \tag{8}$$

Let us bring the equation into a dimensionless form with the help of the change of variables:

$$\xi = \frac{z}{\Delta H}, \quad \alpha = k\Delta H, \quad \tilde{U}_0 = \frac{U_0}{U_m},$$

$$\tilde{N} = \frac{N}{N_0}, \quad C = \frac{c}{U_m}, \quad \Psi = \frac{\psi}{U_m \Delta H},$$

where ΔH is the half-thickness of thermocline, N_0 is the maximum value of buoyancy frequency, and $U_m = U_{\max} + U_{\min}$. For the given experiments, the values of these parameters are shown in Table 1.

Then, Eq. (7) takes the form

$$\frac{\partial^2 \mathbf{\Psi}}{\partial \xi^2} - \alpha^2 \mathbf{\Psi} + \frac{R\tilde{N}^2(\xi)}{(\tilde{U}_0(\xi) - C)^2}\mathbf{\Psi} - \frac{\tilde{U}_0''(\xi)}{(\tilde{U}_0(\xi) - C)}\mathbf{\Psi} = 0 \tag{9}$$

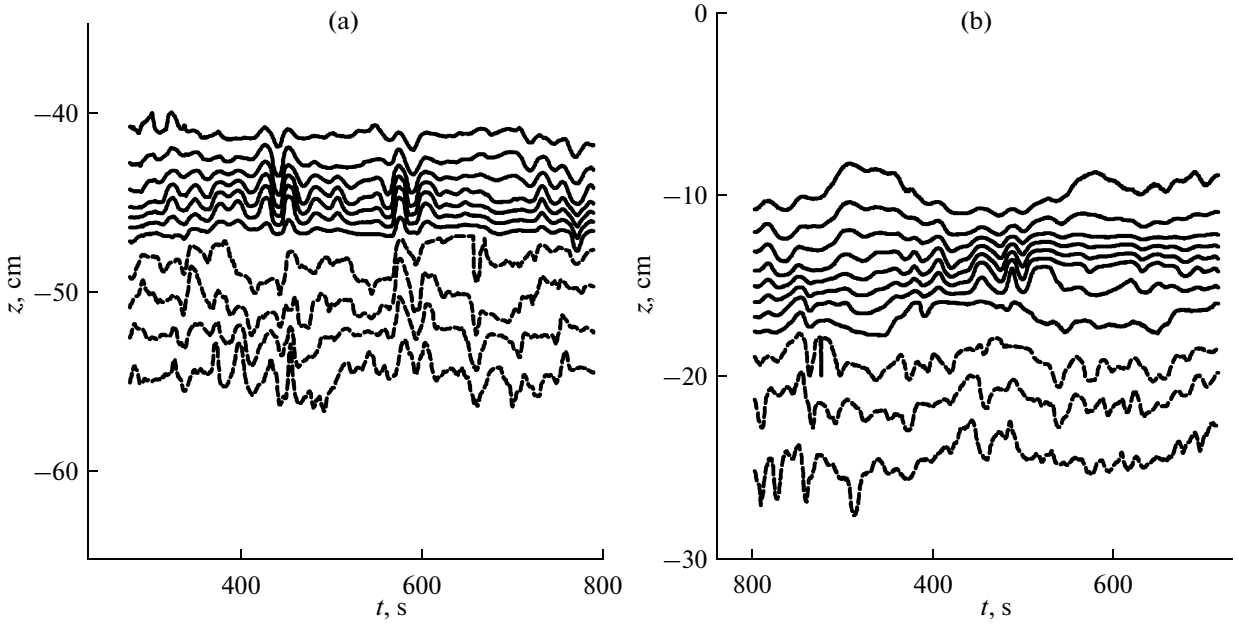

Fig. 3. Examples of the time section of temperature field for (a) Series D and (b) Series S2.

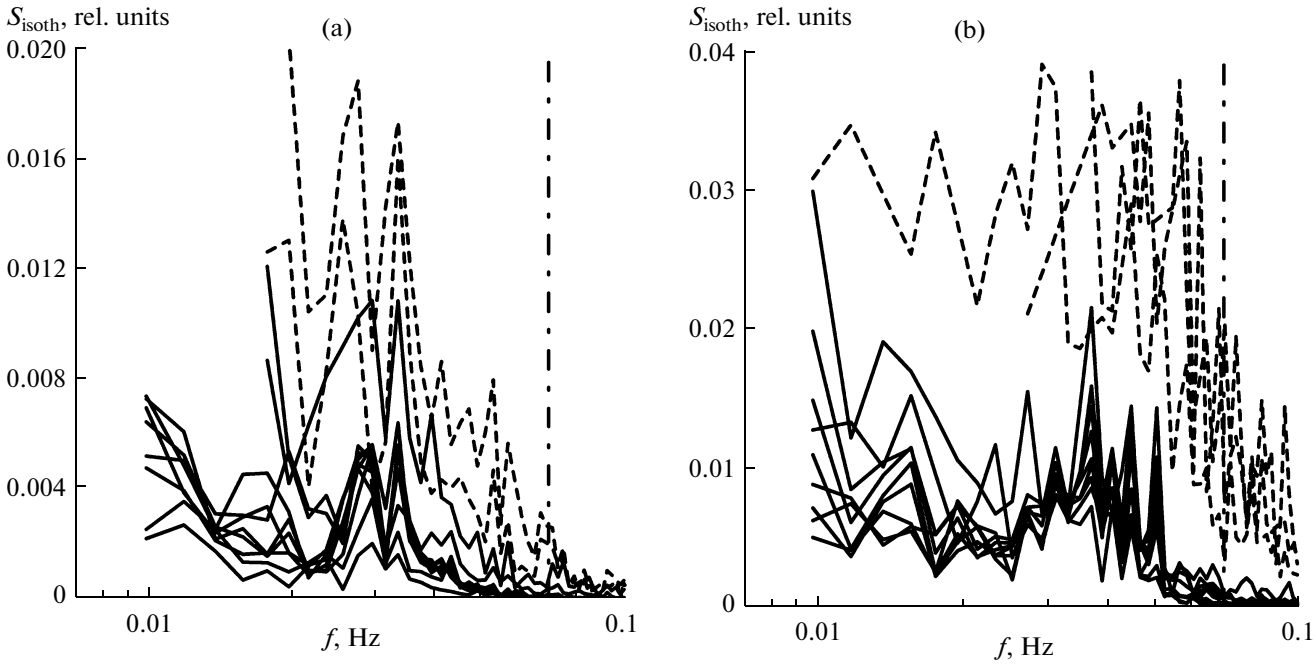

Fig. 4. Spectra of isotherms for the rate of liquid outflow from the collector model of $V_0 = 100$ cm/s ((a) for Series D and (b) for Series S1). The dashed and dotted line denotes the value of buoyancy frequency.

with the boundary conditions at the bottom $\xi = \xi_d$ and surface $\xi = \xi_u$:

$$\psi(\xi_u) = \psi(\xi_d) = 0. \quad (10)$$

In Eq. (9) we have

$$\tilde{N}^2(\xi) = \frac{1}{ch^2(\xi - \xi^*)}, \quad \tilde{U}_0(\xi) = \frac{1}{2}(1 - \beta\, th(\gamma\xi)).$$

Thus, Eq. (9) includes four main dimensionless parameters: a parameter conditionally called the global Richardson number $R = \frac{N_0^2(\Delta H)^2}{U_m^2}$, the ratio of characteristic scales of the thermocline and the jet $\gamma = \left(\frac{\Delta H}{\Delta h}\right)$, the dimensionless embedding of the jet relative

to the thermocline center $\xi^* = = \frac{z^*}{\Delta H}$, and the velocity defect $\beta = \frac{U_{\max} - U_{\min}}{U_{\max} + U_{\min}}$.

The values of these parameters used in numerical calculations are given in Table 1.

4.2. Dispersion Characteristics of Internal Waves in Stratified Liquid in the Presence of Jet Streams

To determine the dispersion characteristics of internal waves, we solve boundary problem (9)–(10) for eigenvalues and eigenfunctions. In this case, the solution to Eq. (9) is represented as a superposition of two linearly independent functions

$$\Psi(\xi) = A\varphi_1(\xi) + B\varphi_2(\xi),$$

where $\varphi_1(\xi)$ and $\varphi_2(\xi)$ are solutions to Eq. (9) with $\varphi_1(0) = 1, \varphi_1'(0) = 0$ and $\varphi_2(0) = 0, \varphi_2'(0) = 1$.

Boundary conditions (10) yield the linear homogeneous system for the coefficients A and B:

$$A\varphi_1(\xi_u) + B\varphi_2(\xi_u) = 0,$$

$$A\varphi_1(\xi_d) + B\varphi_2(\xi_d) = 0.$$

Since the determinant of this system is equal to zero,

$$\varphi_1(\xi_u)\varphi_2(\xi_d) - \varphi_1(\xi_d)\varphi_2(\xi_u) = 0$$

one can numerically determine the dispersion characteristics of internal waves.

Figure 5 shows examples of dispersion characteristics for the first and second modes of internal waves in the stratified basin for a jet stream under the thermocline, corresponding to the global Richardson numbers 1.3, 3, 6, and 10 (Ri = 1.3 is its minimum value and Ri = 10 is its maximum value obtained in the experiment; see Table 1) and in a steady-state stratified liquid.

It can be seen from Fig. 5 that the presence of a jet leads to a significant change in the dispersion characteristics; for example, for $k\Delta H \to \infty$, the curves fall on the asymptotic $\omega = kU_{\max}$, where $U_{\max}$ is the maximum value of the velocity of the jet stream. This asymptotic corresponds to the flow waves on jet stream in liquid without stratification. Here, for the first mode, the smaller the Richardson number is, the faster the fall on the jet asymptotic occurs. The dependences $\omega(k)$ for the second mode fall on this asymptotic at lower values of the dimensionless wave number. The structure of modes was calculated for the average frequency of the interval corresponding to the spectral peak $\omega \approx \omega_0 = 0.035$ Hz or $\frac{\omega}{N_0} \approx 0.5$.

Figure 6 shows the structure of the first and second modes in no-jet and jet conditions in the stratified basin. It can be seen that the structure of the first mode remained almost unchanged, while one of the maxima of the second mode shifted from the thermocline to the jet area. Thus, at the generation frequency, the first mode has a maximum localized near the thermocline and the second mode has a clearly expressed maximum in the jet and a weak maximum in the thermocline area. The jet maximum of the second mode (induced by the jet) allowed us to explain the specific features of the structure of the internal wave field (see Subsection 4.3).

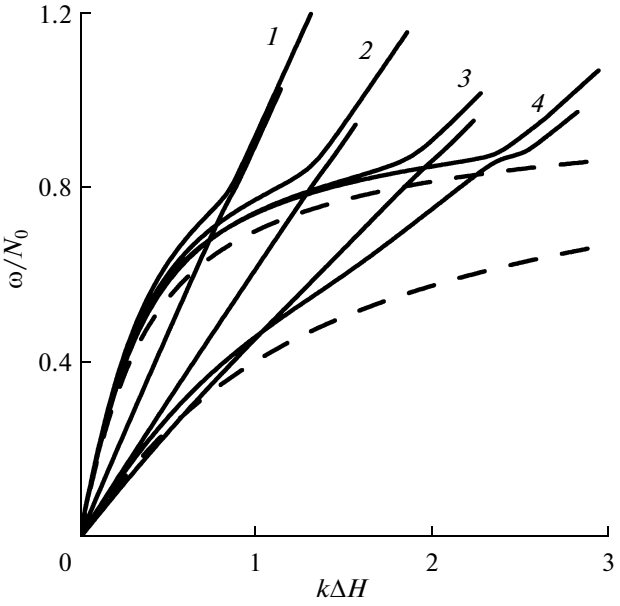

Fig. 5. Dispersion characteristics for the first and second modes at (*1*) Ri = 1.3, (*2*) Ri = 3, (*3*) Ri = 6, and (*4*) Ri = 10. The dotted lines denote dispersion characteristics for the first and second modes in no-jet conditions.

Based on dispersion curves calculated for each experiment in the stratification regime with shallow thermocline, we estimated the phase and group velocities and wavelengths in a frequency range corresponding to the spectral peak; i.e., 0.02–0.05 Hz. They are given in Table 2.

The group velocities of perturbations were compared with the velocities of their propagation obtained experimentally. The velocities of perturbations were determined based on experimental data in the following way.

We compared the velocities of surface perturbations $V(t)$ measured by the PTV method in Series S1 and S2 (Figs. 7, 8b) with measured oscillations of temperature $T(t)$ (Figs. 7, 8a) fixed by a sensor located in the midthermocline. The length of the time shift of the two signals $V(t)$ and $T(t)$ were estimated visually by comparing the implementations and the determination of the time interval between the appearance of

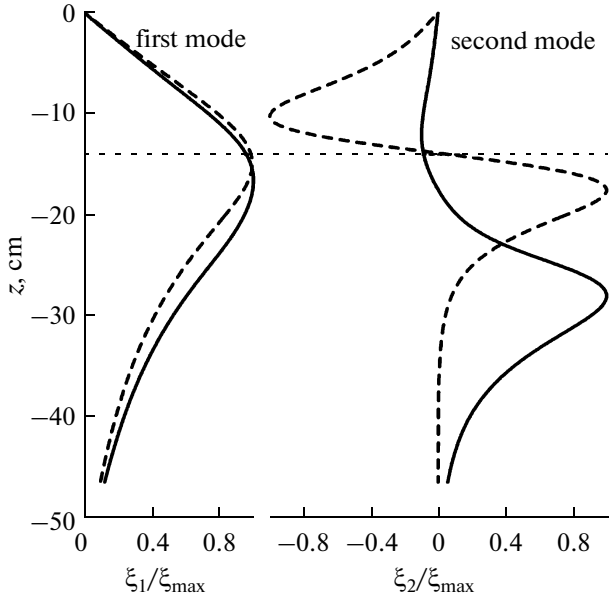

Fig. 6. Structure of the first and second modes in the presence of jet under the thermocline (solid line) and in steady-state stratified liquid (dotted line).

clearly expressed oscillations on these dependences. The dotted lines in Figs. 7, 8a, and 8b indicate the approximately determined (from the plots) start time that perturbations caused by the flow from the collector model are registered. In Series S1 (see the example in Fig. 7), the perturbations first had reached the temperature sensors and only then were the perturbations of surface currents fixed in the observation area. The opposite takes place in Series S2 (see the example in Fig. 8).

Based on the time delay determined in this way, we estimated the perturbation propagation rates. They are shown in Figs. 9 and 10 for different rates of liquid outflow from the collector model and denoted by triangles.

The solid lines in Figs. 9 and 10 indicate the theoretical dependences of group velocities of the first mode of the liquid outflow rate from the collector. The upper curves correspond to group velocities of perturbations at the frequency 0.02 Hz and the lower curves correspond to minimum values of group velocity of the frequency range 0.02–0.05 Hz. One can see that the theory and experiment are very consistent, which confirms the interpretation of observed oscillations of temperature and velocity perturbations on the surface as internal wave fields.

4.3. Mode Structure of Internal Waves

The bimodal shape of the profile of dispersion in isotherm shifts is typical for the mixed regime of perturbations of internal waves, when the first and second modes simultaneously exist. Here, the presence of the first mode is revealed by expressed thermocline oscillations, while the sharply increased amplitudes of oscillations in the jet can point to the second mode. To check this hypothesis, we performed a mode analysis of the experimentally obtained field of isotherm shifts. The vertical structure of this field is represented as an expansion with respect to the first characteristic modes of internal waves in the stratified liquid with a jet over the thermocline; these modes were determined in Subsection 4.2 by solving the boundary problem.

Let us note that the form of eigenfunctions of the first and second modes depends on their frequency. This frequency was chosen based on the following considerations. The measurement data show that the oscillation spectrum has an expressed maximum (see Fig. 4). The eigenfunctions were calculated at a frequency corresponding to this spectral peak with $\omega \approx \omega_0 = 0.035$ Hz. Then, the expansion of the field structure with respect to modes can be sought in the form

$$\xi(z, t) = A(t)\varphi_1(z, \omega_0, k_1(\omega_0)) + B(t)\varphi_2(z, \omega_0, k_2(\omega_0)),$$

where φ_1 and φ_2 are the characteristic modes of the system taken at a frequency corresponding to the spectral peak. The characteristic modes are normalized so that the maxima were equal to 1 (see Figs. 11, 12). In

Table 2.

Series of experiments	S1	S1	S1	S1	S2	S2	S2	S2
Outflow rate (cm/s)	40	70	100	150	40	70	100	150
Phase velocities of perturbations (cm/s)	3.19–1.87	3.22–0.86	3.36–1.2	2.94–0.88	3.76–1.89	3.86–2.59	3.90–3.22	3.47–2.96
Group velocities of perturbations (cm/s)	2.41–0.61	2.82–0.04	2.43–0.13	2.02–0.09	3.03–0.58	3.32–1.21	3.23–1.97	3.11–2.05
Wavelengths of perturbations (cm)	162–43	160–18	160–23	148–18	187–38	230–62	227–97	230–97

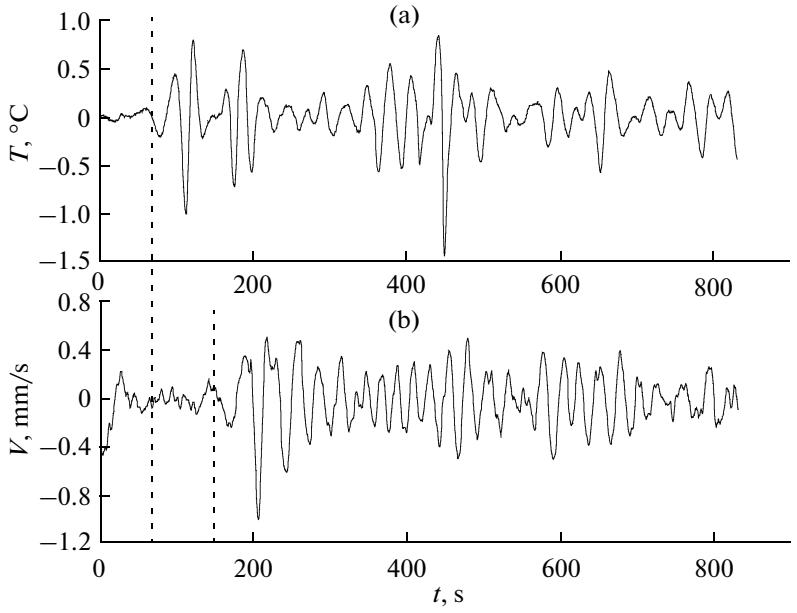

Fig. 7. Experimental results of Series S1 (outflow rate $V_0 = 40$ cm/s): (a) temperature oscillations in the thermocline $T(t)$ and (b) surface velocity $V(t)$.

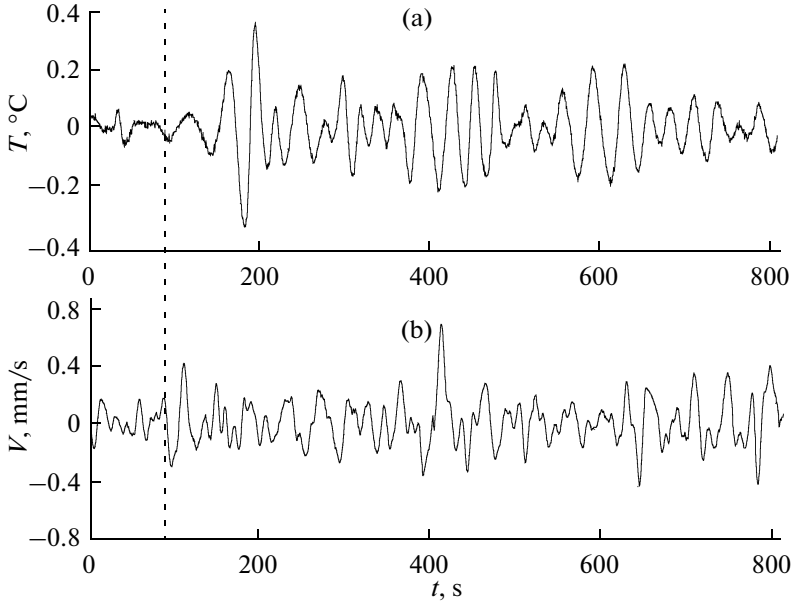

Fig. 8. Experimental results of Series S2 (outflow rate $V_0 = 40$ cm/s): (a) temperature oscillations in the thermocline $T(t)$ and (b) surface velocity $V(t)$.

this case, the dependences $A(t)$ and $B(t)$ show the time dependences of isotherm-shift maxima in the first and second modes.

The coefficients $A(t)$ and $B(t)$ were determined by approximating the dependence of the isotherm shift on depth by the first two modes of the system using the method of least squares. In this case, the coefficients $A(t)$ and $B(t)$ were determined by the system

$$A(t)\sum_{i=1}^{N}\varphi_1^2(z_i) + B(t)\sum_{i=1}^{N}\varphi_1(z_i)\varphi_2(z_i) = \sum_{i=1}^{N}\varphi_1(z_i)\xi(z_i,t),$$

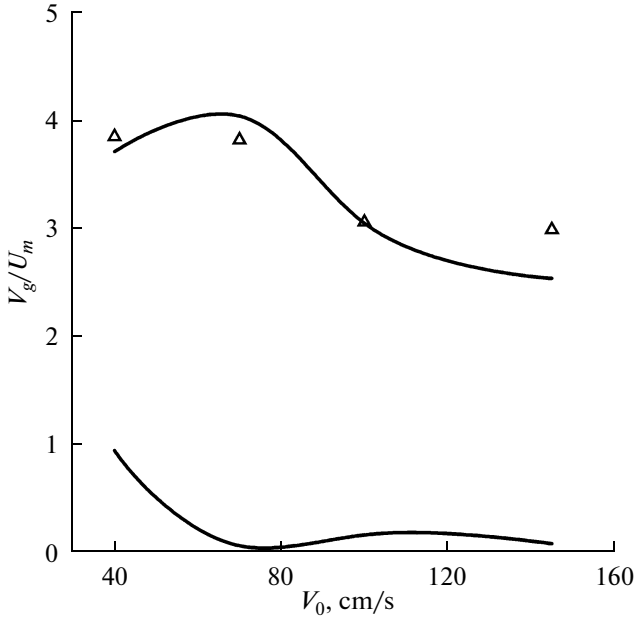

Fig. 9. Corridor of possible values of the group velocity of perturbations in the frequency range of 0.02–0.05 Hz for all rates of liquid outflow from the collector model (Series S1). The triangles denote the velocity values obtained experimentally.

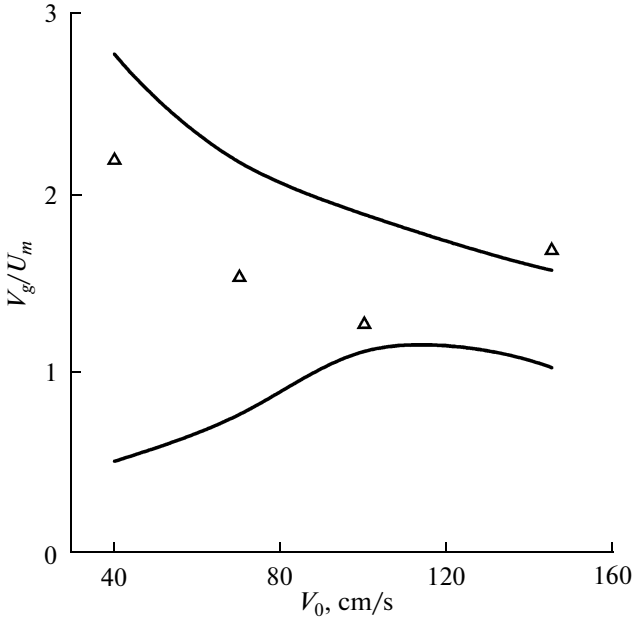

Fig. 10. Corridor of possible values of the group velocity of perturbations in the frequency range of 0.02–0.05 Hz for all rates of liquid outflow from the collector model (Series S2). The triangles denote the velocity values obtained experimentally.

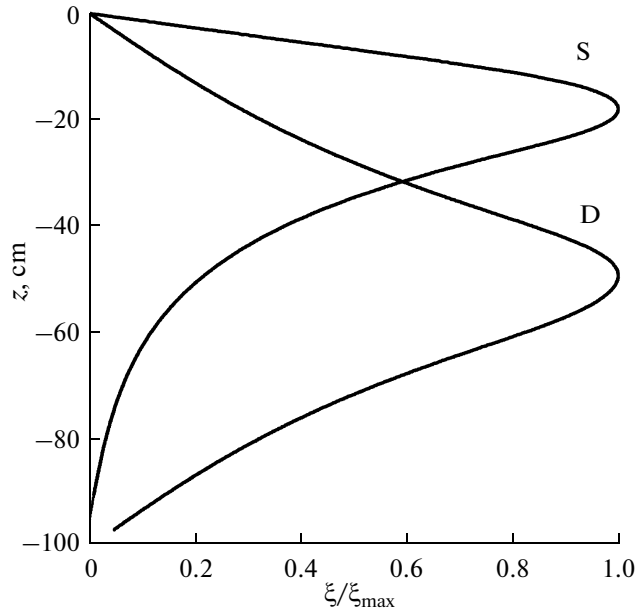

Fig. 11. Example of the structure of the first mode for different stratification regimes.

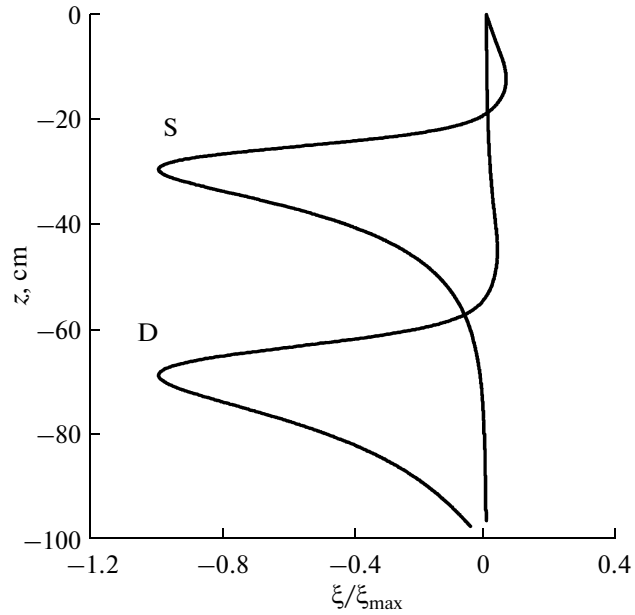

Fig. 12. Example of the structure of the second mode for different stratification regimes.

$$A(t)\sum_{i=1}^{N}\varphi_1(z_i)\varphi_2(z_i) + B(t)\sum_{i=1}^{N}\varphi_2^2(z_i) = \sum_{i=1}^{N}\varphi_2(z_i)\xi(z_i,t),$$

where z_i are the grid points where approximation is used (their number corresponds to the number of isotherms).

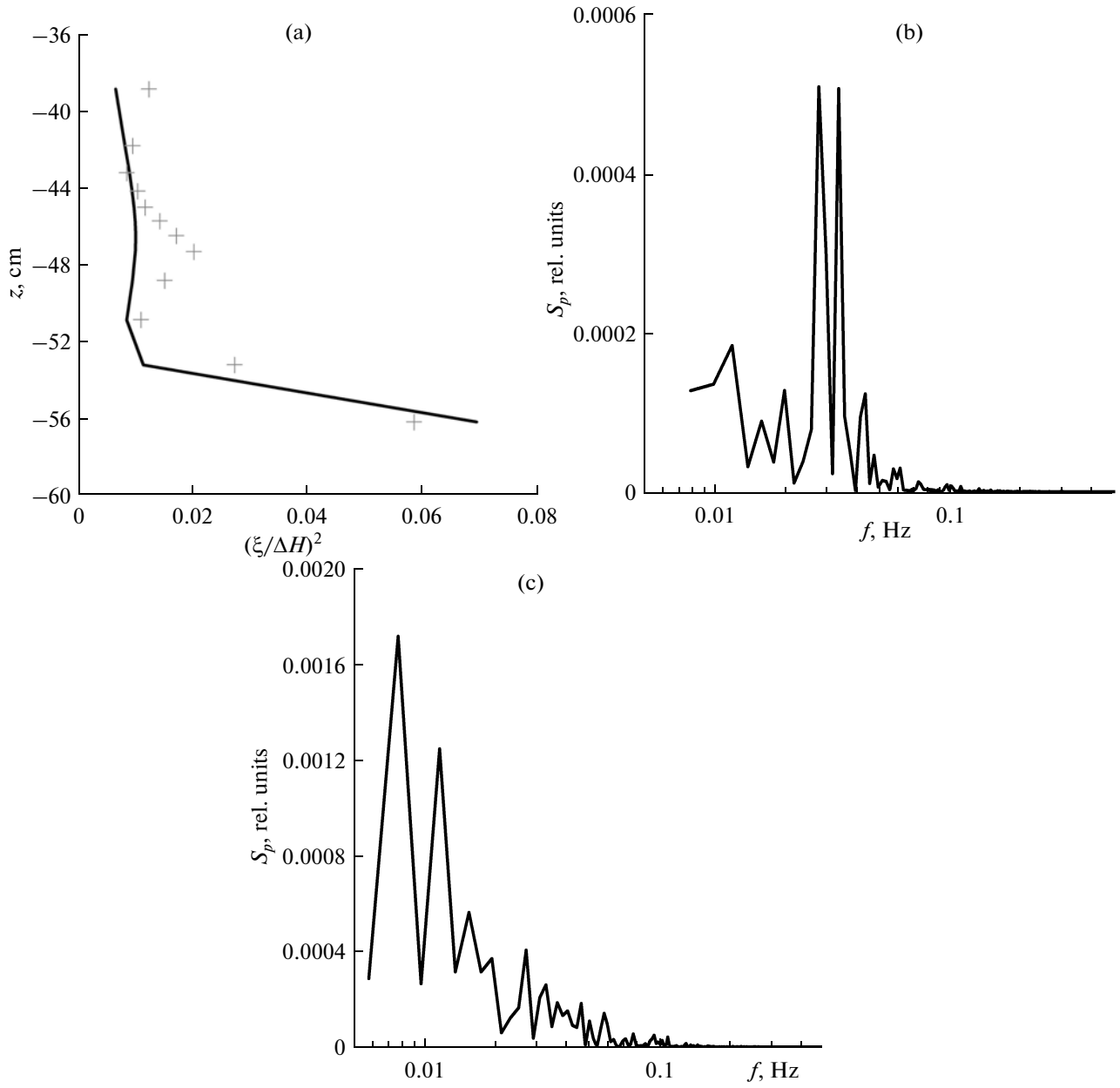

Fig. 13. Experimental dependence of the square isotherm shifts (crosses) and its approximation by the two first modes with the rms method (solid line) for the rate of liquid outflow from (a) the collector model of 100 cm/s and spectra of the expansion coefficients of the vertical structure of internal wave field with respect to (b) the first and (c) the second mode (Series D).

Figures 13 and 14a show the experimental profile of the dispersion of isotherm shifts and its approximation by the superposition of the first and second modes. It can be seen from the figures that the expansion of the field structure with respect to the first two modes yields a satisfactory agreement with experimental data.

Figures 13, 14b, and 14c show the spectra of oscillation amplitudes at the first and second modes $A(t)$ and $B(t)$. The spectrum of the coefficient $A(t)$, which determines the efficiency of actuation of the first mode, has an expressed peak in the frequency range from 0.02 to 0.05 Hz. This type of spectrum is consistent with the spectra of oscillations of isotherms in the thermocline (shown by solid lines in Fig. 4) because the maximum of the first mode is located near the thermocline center and the coefficient $A(t)$ mainly describes the thermocline shift. At the same time, the coefficient $B(t)$ has a broadband spectrum. It is consistent with the spectra of isotherm oscillations in the jet (shown by a dotted line in Fig. 4) because the maximum of the second mode is located in the jet and the coefficient $B(t)$ mainly describes the jet oscillations

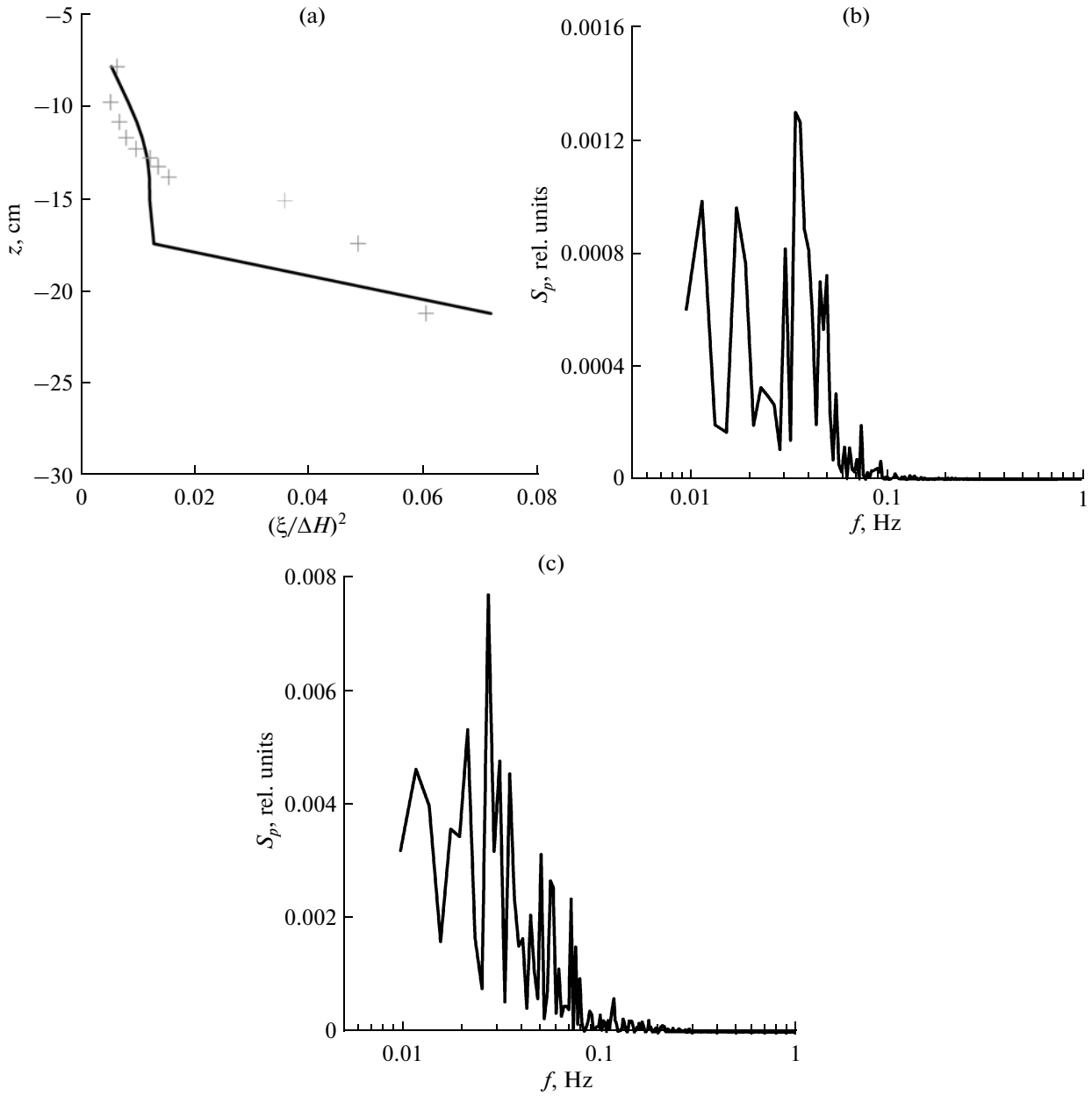

Fig. 14. Experimental dependence of the square isotherm shifts (crosses) and its approximation by the two first modes with the rms method (solid line) for the rate of liquid outflow from (a) the collector model of 70 cm/s and spectra of the expansion coefficients of the vertical structure of internal wave field with respect to (b) the first and (c) the second mode (Series S1).

with a broadband spectrum induced by turbulent fluctuations.

Let us note that the spectral density of the oscillation power of $B(t)$ is higher than that of $A(t)$. This is caused by the fact that the amplitude of isotherm shifts in the jet significantly exceeds the amplitude of isotherm shifts in the thermocline.

5. CONCLUSIONS

The laboratory experiments performed in the LTSR indicated that the interaction between a buoyant jet and thermocline leads to the generation of short-period internal waves. This study provides a detailed analysis of the mode structure of the field of internal waves and their dispersion properties and determines the perturbation velocities at the surface. The typical amplitude of oscillations in the thermocline constituted 1 cm, and the characteristic frequency was 0.035 Hz. One feature of these experiments is that they were performed in large-simulation conditions relative to typical collectors of deepwater sink in a coastal area. The coefficient of simulation was 1 : 27 with respect to the spatial coordinate and

9 : 1 with respect to the frequency. Thus, in typical field conditions, one can expect a range of oscillations in the pycnocline of 60 cm with frequencies of 0.004 Hz.

ACKNOWLEDGMENTS

We are grateful to academician A.V. Gaponov-Grekhov, professor K.D. Sabinin, and doctor O.A. Druzhinin for their useful discussions. This study was supported by the Russian Foundation for Basic Research, project nos. 06-05-64473, 06-05-64890, 07-05-00565a, 08-05-97013r_povolzhie_a, 09-05-00779a, 09-05-00487, and 09-05-00368, as well as by the Foundation for Scientific Schools, project no. NSh1244.2008.2.

REFERENCES

1. B. R. Morton, G. I. Taylor, and J. S. Turner, Turbulent Gravitational Convection from Maintained and Instantaneous Sources, Proc. Roy. Soc. London, **A234**, 1–23 (1956).
2. J. Turner, *Buoyancy Effects in Fluids* (Mir, Moscow, 1977) [in Russian].
3. C. Y. Koh and H. N. Brooks, "Fluid Mechanics of Waste-Water Disposal in the Ocean," Annu. Rev. Fluid Mech. **8**, 187–211 (1975).
4. V. G. Bondur, V. M. Zhurbas, and Yu. V. Grebenyuk, "Mathematical Modeling of Turbulent Jets of Deep-Water Sewage Discharge into Coastal Basins," Okeanologiya **46** (6), 805–820 (2006) [Oceanology **46** (6), 757–771 (2006)].
5. V. G. Bondur, V. M. Zhurbas, and Yu. V. Grebenyuk, "Modeling and Experimental Research of Turbulent Jet Propagation in the Stratified Environment of Coastal Water Areas," Okeanologiya **49** (5) 1–13 (2009) [Oceanology **49** (5), 595–606 (2009)].
6. V. Bondur, R. Keeler, and D. Vithanage, "Sea Truth Measurements for Remote Sensing of Littoral Water," Sea Technology, No. 4, 53–58 (2004).
7. V. G. Bondur, "Aerospace Methods in Modern Oceanology," in *New Ideas in Oceanology*, Vol. 1: *Physics. Chemistry. Biology*, (Nauka, Moscow, 2004), pp. 55–117 [in Russian].
8. V. Bondur, V. G. Bondur, "Complex Satellite Monitoring of Coastal Water Areas," in *Proc. of 31 Int. Symp. on Remote Sensing of Environment* (St. Petersburg, 2005).
9. V. Bondur, R. Keeler, and C. Gibson, "Optical Satellite Imagery Detection of Internal Wave Effects from a Submerged Turbulent Outfall in the Stratified Ocean," GRL **32**, L12610, doi: 10.1029/2005GL022390 (2005).
10. V. G. Bondur and Yu. V. Grebenyuk, "Remote Indication of Anthropogenic Impacts on the Marine Environment Caused by Deep-Water Sewage Discharge: Modeling and Experiment," Issled. Zemli Kosmosa, No. 6, 1–19 (2001).
11. V. G. Bondur, Yu. V. Grebenyuk, E. V. Ezhova, et al., "Surface Manifestations of Internal Waves Investigated by a Subsurface Buoyant Jet: 1. The Mechanism of Internal-Wave Generation," Izv. Akad. Nauk, Fiz. Atmos. Okeana **45** (6), 833–845 (2009) [Izv., Atmos. Ocean. Phys. **45** 779–790 (2009)].
12. Yu. I. Troitskaya, D. A. Sergeev, E. V. Ezhova, et al., "Self-induced Internal Waves Excited by Buoyant Plumes in a Stratified Tank," Dokl. Akad. Nauk 2008 **419** (5), 691–695 [Dokl. Earth Sci. (Engl. Transl.), **419A**, 506–510 (2008)].
13. Yu. I. Troitskaya, D. A. Sergeev, E. V. Ezhova, et al., *Large-Scale Laboratory Modeling of Inland Waves Excited by Deep-Water Collectors of Sewage Discharge*, Preprint IPF RAN No. 751 (Nizhnii Novgorod, 2008) [in Russian].
14. R. J. Adrian, "Particle Imaging Techniques for Experimental Fluid Mechanics," Annu. Rev. Fluid Mech. **23**, 261–304 (1991).
15. V. G. Bondur, Yu. V. Grebenyuk, E. V. Ezhova, et al., Surface Manifestations of Internal Waves Excited by Submerged Turbulent Jet. 3. Surface Manifestations of Internal Waves, Izv. Ros. Akad. Nauk, Fiz. Atm. Okeana, **46** (2010) [Izv., Atmos. Ocean. Phys. **46** (2010)] (in press).
16. E. Gossard and W. Hooke, *Waves in the Atmosphere* (Elsevier, Amsterdam, 1975; Mir, Moscow, 1978).